UC Irvine
UC Irvine Previously Published Works

Title

Measurement of the gamma gamma* -> eta c transition form factor

Permalink

Journal

ISSN

Authors

Lees, JP
Poireau, V
Prencipe, E
et al.

Publication Date

2010

DOI

Copyright Information

Peer reviewed

Measurement of the $\gamma\gamma* \to \eta_c$ transition form factor

J. P. Lees,[1] V. Poireau,[1] E. Prencipe,[1] V. Tisserand,[1] J. Garra Tico,[2] E. Grauges,[2] M. Martinelli,[3a,3b] A. Palano,[3a,3b]
M. Pappagallo,[3a,3b] G. Eigen,[4] B. Stugu,[4] L. Sun,[4] M. Battaglia,[5] D. N. Brown,[5] B. Hooberman,[5] L. T. Kerth,[5]
Yu. G. Kolomensky,[5] G. Lynch,[5] I. L. Osipenkov,[5] T. Tanabe,[5] C. M. Hawkes,[6] N. Soni,[6] A. T. Watson,[6] H. Koch,[7]
T. Schroeder,[7] D. J. Asgeirsson,[8] C. Hearty,[8] T. S. Mattison,[8] J. A. McKenna,[8] M. Barrett,[9] A. Khan,[9] A. Randle-Conde,[9]
V. E. Blinov,[10] A. R. Buzykaev,[10] V. P. Druzhinin,[10] V. B. Golubev,[10] A. P. Onuchin,[10] S. I. Serednyakov,[10]
Yu. I. Skovpen,[10] E. P. Solodov,[10] K. Yu. Todyshev,[10] A. N. Yushkov,[10] M. Bondioli,[11] S. Curry,[11] D. Kirkby,[11]
A. J. Lankford,[11] P. Lund,[11] M. Mandelkern,[11] E. C. Martin,[11] D. P. Stoker,[11] H. Atmacan,[12] J. W. Gary,[12] F. Liu,[12]
O. Long,[12] G. M. Vitug,[12] Z. Yasin,[12] V. Sharma,[13] C. Campagnari,[14] T. M. Hong,[14] D. Kovalskyi,[14] J. D. Richman,[14]
A. M. Eisner,[15] C. A. Heusch,[15] J. Kroseberg,[15] W. S. Lockman,[15] A. J. Martinez,[15] T. Schalk,[15] B. A. Schumm,[15]
A. Seiden,[15] L. O. Winstrom,[15] C. H. Cheng,[16] D. A. Doll,[16] B. Echenard,[16] D. G. Hitlin,[16] P. Ongmongkolkul,[16]
F. C. Porter,[16] A. Y. Rakitin,[16] R. Andreassen,[17] M. S. Dubrovin,[17] G. Mancinelli,[17] B. T. Meadows,[17] M. D. Sokoloff,[17]
P. C. Bloom,[18] W. T. Ford,[18] A. Gaz,[18] J. F. Hirschauer,[18] M. Nagel,[18] U. Nauenberg,[18] J. G. Smith,[18] S. R. Wagner,[18]
R. Ayad,[19,*] W. H. Toki,[19] E. Feltresi,[20] A. Hauke,[20] H. Jasper,[20] T. M. Karbach,[20] J. Merkel,[20] A. Petzold,[20] B. Spaan,[20]
K. Wacker,[20] M. J. Kobel,[21] K. R. Schubert,[21] R. Schwierz,[21] D. Bernard,[22] M. Verderi,[22] P. J. Clark,[23] S. Playfer,[23]
J. E. Watson,[23] M. Andreotti,[24a,24b] D. Bettoni,[24a] C. Bozzi,[24a] R. Calabrese,[24a,24b] A. Cecchi,[24a,24b] G. Cibinetto,[24a,24b]
E. Fioravanti,[24a,24b] P. Franchini,[24a,24b] E. Luppi,[24a,24b] M. Munerato,[24a,24b] M. Negrini,[24a,24b] A. Petrella,[24a,24b]
L. Piemontese,[24a] V. Santoro,[24a,24b] R. Baldini-Ferroli,[25] A. Calcaterra,[25] R. de Sangro,[25] G. Finocchiaro,[25] M. Nicolaci,[25]
S. Pacetti,[25] P. Patteri,[25] I. M. Peruzzi,[25,†] M. Piccolo,[25] M. Rama,[25] A. Zallo,[25] R. Contri,[26a,26b] E. Guido,[26a,26b]
M. Lo Vetere,[26a,26b] M. R. Monge,[26a,26b] S. Passaggio,[26a] C. Patrignani,[26a,26b] E. Robutti,[26a] S. Tosi,[26a,26b] B. Bhuyan,[27]
M. Morii,[28] A. Adametz,[29] J. Marks,[29] S. Schenk,[29] U. Uwer,[29] F. U. Bernlochner,[30] H. M. Lacker,[30] T. Lueck,[30] A. Volk,[30]
P. D. Dauncey,[31] M. Tibbetts,[31] P. K. Behera,[32] U. Mallik,[32] C. Chen,[33] J. Cochran,[33] H. B. Crawley,[33] L. Dong,[33]
W. T. Meyer,[33] S. Prell,[33] E. I. Rosenberg,[33] A. E. Rubin,[33] Y. Y. Gao,[34] A. V. Gritsan,[34] Z. J. Guo,[34] N. Arnaud,[35]
M. Davier,[35] D. Derkach,[35] J. Firmino da Costa,[35] G. Grosdidier,[35] F. Le Diberder,[35] A. M. Lutz,[35] B. Malaescu,[35]
P. Roudeau,[35] M. H. Schune,[35] J. Serrano,[35] V. Sordini,[35,‡] A. Stocchi,[35] L. Wang,[35] G. Wormser,[35] D. J. Lange,[36]
D. M. Wright,[36] I. Bingham,[37] J. P. Burke,[37] C. A. Chavez,[37] J. R. Fry,[37] E. Gabathuler,[37] R. Gamet,[37] D. E. Hutchcroft,[37]
D. J. Payne,[37] C. Touramanis,[37] A. J. Bevan,[38] F. Di Lodovico,[38] R. Sacco,[38] M. Sigamani,[38] G. Cowan,[39]
S. Paramesvaran,[39] A. C. Wren,[39] D. N. Brown,[40] C. L. Davis,[40] A. G. Denig,[41] M. Fritsch,[41] W. Gradl,[41] A. Hafner,[41]
K. E. Alwyn,[42] D. Bailey,[42] R. J. Barlow,[42] G. Jackson,[42] G. D. Lafferty,[42] T. J. West,[42] J. Anderson,[43] A. Jawahery,[43]
D. A. Roberts,[43] G. Simi,[43] J. M. Tuggle,[43] C. Dallapiccola,[44] E. Salvati,[44] R. Cowan,[45] D. Dujmic,[45] P. H. Fisher,[45]
G. Sciolla,[45] R. K. Yamamoto,[45] M. Zhao,[45] P. M. Patel,[46] S. H. Robertson,[46] M. Schram,[46] P. Biassoni,[47a,47b]
A. Lazzaro,[47a,47b] V. Lombardo,[47a] F. Palombo,[47a,47b] S. Stracka,[47a,47b] L. Cremaldi,[48] R. Godang,[48,§] R. Kroeger,[48]
P. Sonnek,[48] D. J. Summers,[48] H. W. Zhao,[48] X. Nguyen,[49] M. Simard,[49] P. Taras,[49] G. De Nardo,[50a,50b]
D. Monorchio,[50a,50b] G. Onorato,[50a,50b] C. Sciacca,[50a,50b] G. Raven,[51] H. L. Snoek,[51] C. P. Jessop,[52] K. J. Knoepfel,[52]
J. M. LoSecco,[52] W. F. Wang,[52] L. A. Corwin,[53] K. Honscheid,[53] R. Kass,[53] J. P. Morris,[53] A. M. Rahimi,[53] S. J. Sekula,[53]
N. L. Blount,[54] J. Brau,[54] R. Frey,[54] O. Igonkina,[54] J. A. Kolb,[54] M. Lu,[54] R. Rahmat,[54] N. B. Sinev,[54] D. Strom,[54]
J. Strube,[54] E. Torrence,[54] G. Castelli,[55a,55b] N. Gagliardi,[55a,55b] M. Margoni,[55a,55b] M. Morandin,[55a] M. Posocco,[55a]
M. Rotondo,[55a] F. Simonetto,[55a,55b] R. Stroili,[55a,55b] P. del Amo Sanchez,[56] E. Ben-Haim,[56] G. R. Bonneaud,[56] H. Briand,[56]
J. Chauveau,[56] O. Hamon,[56] Ph. Leruste,[56] G. Marchiori,[56] J. Ocariz,[56] A. Perez,[56] J. Prendki,[56] S. Sitt,[56] M. Biasini,[57a,57b]
E. Manoni,[57a,57b] C. Angelini,[58a,58b] G. Batignani,[58a,58b] S. Bettarini,[58a,58b] G. Calderini,[58a,58b,||] M. Carpinelli,[58a,58b,¶]
A. Cervelli,[58a,58b] F. Forti,[58a,58b] M. A. Giorgi,[58a,58b] A. Lusiani,[58a,58c] N. Neri,[58a,58b] E. Paoloni,[58a,58b] G. Rizzo,[58a,58b]
J. J. Walsh,[58a] D. Lopes Pegna,[59] C. Lu,[59] J. Olsen,[59] A. J. S. Smith,[59] A. V. Telnov,[59] F. Anulli,[60a] E. Baracchini,[60a,60b]
G. Cavoto,[60a] R. Faccini,[60a,60b] F. Ferrarotto,[60a] F. Ferroni,[60a,60b] M. Gaspero,[60a,60b] P. D. Jackson,[60a] L. Li Gioi,[60a]
M. A. Mazzoni,[60a] G. Piredda,[60a] F. Renga,[60a,60b] M. Ebert,[61] T. Hartmann,[61] T. Leddig,[61] H. Schröder,[61] R. Waldi,[61]
T. Adye,[62] B. Franek,[62] E. O. Olaiya,[62] F. F. Wilson,[62] S. Emery,[63] G. Hamel de Monchenault,[63] G. Vasseur,[63] Ch. Yèche,[63]
M. Zito,[63] M. T. Allen,[64] D. Aston,[64] D. J. Bard,[64] R. Bartoldus,[64] J. F. Benitez,[64] C. Cartaro,[64] R. Cenci,[64] J. P. Coleman,[64]
M. R. Convery,[64] J. C. Dingfelder,[64] J. Dorfan,[64] G. P. Dubois-Felsmann,[64] W. Dunwoodie,[64] R. C. Field,[64]
M. Franco Sevilla,[64] B. G. Fulsom,[64] A. M. Gabareen,[64] M. T. Graham,[64] P. Grenier,[64] C. Hast,[64] W. R. Innes,[64]
J. Kaminski,[64] M. H. Kelsey,[64] H. Kim,[64] P. Kim,[64] M. L. Kocian,[64] D. W. G. S. Leith,[64] S. Li,[64] B. Lindquist,[64] S. Luitz,[64]
V. Luth,[64] H. L. Lynch,[64] D. B. MacFarlane,[64] H. Marsiske,[64] R. Messner,[64,**] D. R. Muller,[64] H. Neal,[64] S. Nelson,[64]

C. P. O'Grady,[64] I. Ofte,[64] M. Perl,[64] B. N. Ratcliff,[64] A. Roodman,[64] A. A. Salnikov,[64] R. H. Schindler,[64] J. Schwiening,[64] A. Snyder,[64] D. Su,[64] M. K. Sullivan,[64] K. Suzuki,[64] S. K. Swain,[64] J. M. Thompson,[64] J. Va'vra,[64] A. P. Wagner,[64] M. Weaver,[64] C. A. West,[64] W. J. Wisniewski,[64] M. Wittgen,[64] D. H. Wright,[64] H. W. Wulsin,[64] A. K. Yarritu,[64] C. C. Young,[64] V. Ziegler,[64] X. R. Chen,[65] H. Liu,[65] W. Park,[65] M. V. Purohit,[65] R. M. White,[65] J. R. Wilson,[65] M. Bellis,[66] P. R. Burchat,[66] A. J. Edwards,[66] T. S. Miyashita,[66] S. Ahmed,[67] M. S. Alam,[67] J. A. Ernst,[67] B. Pan,[67] M. A. Saeed,[67] S. B. Zain,[67] N. Guttman,[68] A. Soffer,[68] S. M. Spanier,[69] B. J. Wogsland,[69] R. Eckmann,[70] J. L. Ritchie,[70] A. M. Ruland,[70] C. J. Schilling,[70] R. F. Schwitters,[70] B. C. Wray,[70] J. M. Izen,[71] X. C. Lou,[71] F. Bianchi,[72a,72b] D. Gamba,[72a,72b] M. Pelliccioni,[72a,72b] M. Bomben,[73a,73b] G. Della Ricca,[73a,73b] L. Lanceri,[73a,73b] L. Vitale,[73a,73b] V. Azzolini,[74] N. Lopez-March,[74] F. Martinez-Vidal,[74] D. A. Milanes,[74] A. Oyanguren,[74] J. Albert,[75] Sw. Banerjee,[75] H. H. F. Choi,[75] K. Hamano,[75] G. J. King,[75] R. Kowalewski,[75] M. J. Lewczuk,[75] I. M. Nugent,[75] J. M. Roney,[75] R. J. Sobie,[75] T. J. Gershon,[76] P. F. Harrison,[76] J. Ilic,[76] T. E. Latham,[76] G. B. Mohanty,[76] E. M. T. Puccio,[76] H. R. Band,[77] X. Chen,[77] S. Dasu,[77] K. T. Flood,[77] Y. Pan,[77] R. Prepost,[77] C. O. Vuosalo,[77] and S. L. Wu[77]

[1]*Laboratoire d'Annecy-le-Vieux de Physique des Particules (LAPP), Université de Savoie, CNRS/IN2P3, F-74941 Annecy-Le-Vieux, France*
[2]*Universitat de Barcelona, Facultat de Fisica, Departament ECM, E-08028 Barcelona, Spain*
[3a]*INFN Sezione di Bari, I-70126 Bari, Italy*
[3b]*Dipartimento di Fisica, Università di Bari, I-70126 Bari, Italy*
[4]*University of Bergen, Institute of Physics, N-5007 Bergen, Norway*
[5]*Lawrence Berkeley National Laboratory and University of California, Berkeley, California 94720, USA*
[6]*University of Birmingham, Birmingham, B15 2TT, United Kingdom*
[7]*Ruhr Universität Bochum, Institut für Experimentalphysik 1, D-44780 Bochum, Germany*
[8]*University of British Columbia, Vancouver, British Columbia, Canada V6T 1Z1*
[9]*Brunel University, Uxbridge, Middlesex UB8 3PH, United Kingdom*
[10]*Budker Institute of Nuclear Physics, Novosibirsk 630090, Russia*
[11]*University of California at Irvine, Irvine, California 92697, USA*
[12]*University of California at Riverside, Riverside, California 92521, USA*
[13]*University of California at San Diego, La Jolla, California 92093, USA*
[14]*University of California at Santa Barbara, Santa Barbara, California 93106, USA*
[15]*University of California at Santa Cruz, Institute for Particle Physics, Santa Cruz, California 95064, USA*
[16]*California Institute of Technology, Pasadena, California 91125, USA*
[17]*University of Cincinnati, Cincinnati, Ohio 45221, USA*
[18]*University of Colorado, Boulder, Colorado 80309, USA*
[19]*Colorado State University, Fort Collins, Colorado 80523, USA*
[20]*Technische Universität Dortmund, Fakultät Physik, D-44221 Dortmund, Germany*
[21]*Technische Universität Dresden, Institut für Kern- und Teilchenphysik, D-01062 Dresden, Germany*
[22]*Laboratoire Leprince-Ringuet, CNRS/IN2P3, Ecole Polytechnique, F-91128 Palaiseau, France*
[23]*University of Edinburgh, Edinburgh EH9 3JZ, United Kingdom*
[24a]*INFN Sezione di Ferrara, I-44100 Ferrara, Italy*
[24b]*Dipartimento di Fisica, Università di Ferrara, I-44100 Ferrara, Italy*
[25]*INFN Laboratori Nazionali di Frascati, I-00044 Frascati, Italy*
[26a]*INFN Sezione di Genova, I-16146 Genova, Italy*
[26b]*Dipartimento di Fisica, Università di Genova, I-16146 Genova, Italy*
[27]*Indian Institute of Technology Guwahati, Guwahati, Assam, 781 039, India*
[28]*Harvard University, Cambridge, Massachusetts 02138, USA*
[29]*Universität Heidelberg, Physikalisches Institut, Philosophenweg 12, D-69120 Heidelberg, Germany*
[30]*Humboldt-Universität zu Berlin, Institut für Physik, Newtonstr. 15, D-12489 Berlin, Germany*
[31]*Imperial College London, London, SW7 2AZ, United Kingdom*
[32]*University of Iowa, Iowa City, Iowa 52242, USA*
[33]*Iowa State University, Ames, Iowa 50011-3160, USA*
[34]*Johns Hopkins University, Baltimore, Maryland 21218, USA*
[35]*Laboratoire de l'Accélérateur Linéaire, IN2P3/CNRS et Université Paris-Sud 11, Centre Scientifique d'Orsay, B. P. 34, F-91898 Orsay Cedex, France*
[36]*Lawrence Livermore National Laboratory, Livermore, California 94550, USA*
[37]*University of Liverpool, Liverpool L69 7ZE, United Kingdom*
[38]*Queen Mary, University of London, London, E1 4NS, United Kingdom*
[39]*University of London, Royal Holloway and Bedford New College, Egham, Surrey TW20 0EX, United Kingdom*
[40]*University of Louisville, Louisville, Kentucky 40292, USA*
[41]*Johannes Gutenberg-Universität Mainz, Institut für Kernphysik, D-55099 Mainz, Germany*

[42]*University of Manchester, Manchester M13 9PL, United Kingdom*
[43]*University of Maryland, College Park, Maryland 20742, USA*
[44]*University of Massachusetts, Amherst, Massachusetts 01003, USA*
[45]*Massachusetts Institute of Technology, Laboratory for Nuclear Science, Cambridge, Massachusetts 02139, USA*
[46]*McGill University, Montréal, Québec, Canada H3A 2T8*
[47a]*INFN Sezione di Milano, I-20133 Milano, Italy*
[47b]*Dipartimento di Fisica, Università di Milano, I-20133 Milano, Italy*
[48]*University of Mississippi, University, Mississippi 38677, USA*
[49]*Université de Montréal, Physique des Particules, Montréal, Québec, Canada H3C 3J7*
[50a]*INFN Sezione di Napoli, I-80126 Napoli, Italy*
[50b]*Dipartimento di Scienze Fisiche, Università di Napoli Federico II, I-80126 Napoli, Italy*
[51]*NIKHEF, National Institute for Nuclear Physics and High Energy Physics, NL-1009 DB Amsterdam, The Netherlands*
[52]*University of Notre Dame, Notre Dame, Indiana 46556, USA*
[53]*Ohio State University, Columbus, Ohio 43210, USA*
[54]*University of Oregon, Eugene, Oregon 97403, USA*
[55a]*INFN Sezione di Padova, I-35131 Padova, Italy*
[55b]*Dipartimento di Fisica, Università di Padova, I-35131 Padova, Italy*
[56]*Laboratoire de Physique Nucléaire et de Hautes Energies, IN2P3/CNRS, Université Pierre et Marie Curie-Paris6,*
Université Denis Diderot-Paris7, F-75252 Paris, France
[57a]*INFN Sezione di Perugia, I-06100 Perugia, Italy*
[57b]*Dipartimento di Fisica, Università di Perugia, I-06100 Perugia, Italy*
[58a]*INFN Sezione di Pisa, I-56127 Pisa, Italy*
[58b]*Dipartimento di Fisica, Università di Pisa, I-56127 Pisa, Italy*
[58c]*Scuola Normale Superiore di Pisa, I-56127 Pisa, Italy*
[59]*Princeton University, Princeton, New Jersey 08544, USA*
[60a]*INFN Sezione di Roma, I-00185 Roma, Italy*
[60b]*Dipartimento di Fisica, Università di Roma La Sapienza, I-00185 Roma, Italy*
[61]*Universität Rostock, D-18051 Rostock, Germany*
[62]*Rutherford Appleton Laboratory, Chilton, Didcot, Oxon, OX11 0QX, United Kingdom*
[63]*CEA, Irfu, SPP, Centre de Saclay, F-91191 Gif-sur-Yvette, France*
[64]*SLAC National Accelerator Laboratory, Stanford, California 94309 USA*
[65]*University of South Carolina, Columbia, South Carolina 29208, USA*
[66]*Stanford University, Stanford, California 94305-4060, USA*
[67]*State University of New York, Albany, New York 12222, USA*
[68]*Tel Aviv University, School of Physics and Astronomy, Tel Aviv, 69978, Israel*
[69]*University of Tennessee, Knoxville, Tennessee 37996, USA*
[70]*University of Texas at Austin, Austin, Texas 78712, USA*
[71]*University of Texas at Dallas, Richardson, Texas 75083, USA*
[72a]*INFN Sezione di Torino, I-10125 Torino, Italy*
[72b]*Dipartimento di Fisica Sperimentale, Università di Torino, I-10125 Torino, Italy*
[73a]*INFN Sezione di Trieste, I-34127 Trieste, Italy*
[73b]*Dipartimento di Fisica, Università di Trieste, I-34127 Trieste, Italy*
[74]*IFIC, Universitat de Valencia-CSIC, E-46071 Valencia, Spain*
[75]*University of Victoria, Victoria, British Columbia, Canada V8W 3P6*
[76]*Department of Physics, University of Warwick, Coventry CV4 7AL, United Kingdom*
[77]*University of Wisconsin, Madison, Wisconsin 53706, USA*

We study the reaction $e^+e^- \rightarrow e^+e^-\eta_c$, $\eta_c \rightarrow K_S K^\pm \pi^\mp$ and obtain η_c mass and width values $2982.2 \pm 0.4 \pm 1.6$ MeV/c^2 and $31.7 \pm 1.2 \pm 0.8$ MeV, respectively. We find $\Gamma(\eta_c \rightarrow \gamma\gamma)\mathcal{B}(\eta_c \rightarrow K\bar{K}\pi) = 0.374 \pm 0.009 \pm 0.031$ keV, and measure the $\gamma\gamma* \rightarrow \eta_c$ transition form factor in the momentum transfer range from 2 to 50 GeV^2. The analysis is based on 469 fb^{-1} of integrated luminosity collected at PEP-II with the *BABAR* detector at e^+e^- center-of-mass energies near 10.6 GeV.

*Now at Temple University, Philadelphia, Pennsylvania 19122, USA.

†Also with Università di Perugia, Dipartimento di Fisica, Perugia, Italy.

‡Also with Università di Roma La Sapienza, I-00185 Roma, Italy.

§Now at University of South Alabama, Mobile, Alabama 36688, USA.

‖Also with Laboratoire de Physique Nucléaire et de Hautes Energies, IN2P3/CNRS, Université Pierre et Marie Curie-Paris6, Université Denis Diderot-Paris7, F-75252 Paris, France.

¶Also with Università di Sassari, Sassari, Italy.

**Deceased.

I. INTRODUCTION

In this paper we study the process

$$e^+e^- \rightarrow e^+e^-\eta_c, \tag{1}$$

where the η_c meson ($J^{PC} = 0^{-+}$), the lowest lying charmonium state, is produced via the two-photon production mechanism illustrated in Fig. 1. We measure the differential cross section for this process in the single-tag mode where one of the outgoing electrons[1] is detected (tagged), while the other electron is scattered at a small angle and hence is undetected (untagged). The tagged electron emits a highly off-shell photon with squared momentum transfer $q_1^2 \equiv -Q^2 = (p' - p)^2$, where p and p' are the four-momenta of the initial- and final-state electrons. The momentum transfer squared to the untagged electron (q_2^2) is near zero. The differential cross section $d\sigma(e^+e^- \rightarrow e^+e^-P)/dQ^2$ for pseudoscalar meson (P) production depends on only one form factor $F(Q^2)$, which describes the $\gamma\gamma^* \rightarrow P$ transition. To relate the differential cross section to the transition form factor we use the formulae for the $e^+e^- \rightarrow e^+e^-\pi^0$ cross section in Eqs. (2.1) and (4.5) of Ref. [1].

According to perturbative QCD (pQCD), the transition form factor can be presented as a convolution of a calculable hard scattering amplitude for $\gamma\gamma^* \rightarrow c\bar{c}$ with a nonperturbative light-cone wave function ϕ_{η_c} [2]. The measurement of the form factor allows us to test the pQCD prediction and to obtain information on the shape of the η_c wave function. The Q^2 dependence of the form factor is studied theoretically in Refs. [3,4] using pQCD, and in Ref. [5] using the lattice QCD approach.

The η_c transition form factor was measured by the L3 Collaboration [6] with very small data sample. In this paper we study the $e^+e^- \rightarrow e^+e^-\eta_c$ reaction in the Q^2 range from 2 to 50 GeV^2. The η_c is observed via the $\eta_c \rightarrow K_S K^\pm \pi^\mp$ decay,[2] which allows the η_c to be selected with relatively low background. The η_c two-photon width and branching fractions are not well measured [7]. Therefore, we also study no-tag data ($Q^2 \sim 0$), measure the product $\Gamma(\eta_c \rightarrow \gamma\gamma)\mathcal{B}(\eta_c \rightarrow K\bar{K}\pi)$, and normalize the transition form factor $F(Q^2)$ to $F(0)$. The measured values of the η_c mass and width obtained in different experiments have a large spread [7]. The high statistics no-tag data sample allows us to extract precise values for these parameters.

---

[1] Unless otherwise specified, we use the term "electron" for either an electron or a positron.

[2] The use of charge conjugate reactions is implied throughout unless explicitly stated otherwise.

II. THE *BABAR* DETECTOR AND DATA SAMPLES

We analyze a data sample corresponding to an integrated luminosity of 469 fb^{-1} recorded with the *BABAR* detector [8] at the PEP-II asymmetric-energy storage rings at SLAC. At PEP-II, 9 GeV electrons collide with 3.1 GeV positrons to yield an e^+e^- center-of-mass (c.m.) energy of 10.58 GeV (the $\Upsilon(4S)$ resonance). About 10% of the data used in the present analysis were recorded about 40 MeV below the resonance.

Charged-particle tracking is provided by a five-layer silicon vertex tracker (SVT) and a 40-layer drift chamber (DCH) operating in a 1.5-T axial magnetic field. The transverse momentum resolution is 0.47% at 1 GeV/c. Energies of photons and electrons are measured with a CsI(Tl) electromagnetic calorimeter (EMC) with a resolution of 3% at 1 GeV. Charged-particle identification is provided by specific ionization measurements in the SVT and DCH, and by an internally reflecting ring-imaging Cherenkov detector (DIRC). Electron identification also uses shower shape in the EMC and the ratio of shower energy to track momentum. Muons are identified in the solenoid's instrumented flux return, which consist of iron plates interleaved with resistive plate chambers.

The signal process is simulated with the Monte Carlo (MC) event generator GGResRc. It uses the formula for the differential cross section for pseudoscalar meson production from Ref. [1]. Two samples of signal events are produced: one for no-tag measurement without any kinematic restrictions, and the other with the restrictions on the momentum transfer values to the electrons $Q^2 = -q_1^2 > 1.5$ GeV^2 and $-q_2^2 < 1$ GeV^2. The restriction on Q^2 for the tagged electron corresponds to the detector acceptance. The experimental criteria providing these restrictions for data events will be described in Sec. III. In the simulation of no-tag events we use the form factor

$$F(q_1^2, q_2^2) = \frac{F(0, 0)}{(1 - q_1^2/m_{J/\psi}^2)(1 - q_2^2/m_{J/\psi}^2)} \tag{2}$$

expected in the vector dominance model. The form factor is fixed to the constant value $F(0, 0)$ in the simulation of single-tag events. The produced η_c decays into the
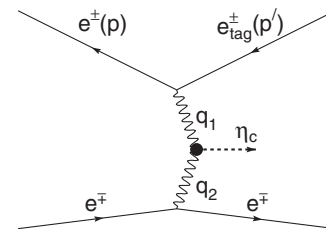

FIG. 1. The Feynman diagram for the $e^+e^- \rightarrow e^+e^-\eta_c$ two-photon production process.
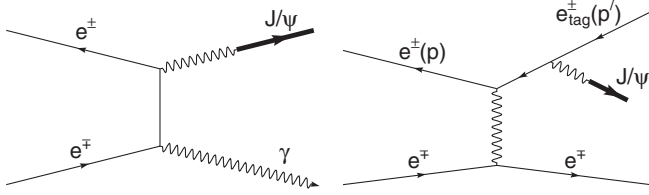
FIG. 2. The Feynman diagrams for the background processes (a) $e^+e^- \rightarrow J/\psi\gamma$, and (b) $e^+e^- \rightarrow e^+e^-J/\psi$.

$K_S K^\pm \pi^\mp$ final state. The simulation uses a three-body phase space distribution to describe this decay.

The GGResRc event generator includes next-to-leading-order radiative corrections to the Born cross section calculated according to Ref. [9]. In particular, it generates extra photons emitted by the initial- and final-state electrons. The formulae from Ref. [9] are modified to take into account the hadron contribution to the vacuum polarization diagrams. The maximum energy of the photon emitted from the initial state is restricted by the requirement[3] $E_\gamma^* < 0.05\sqrt{s}$, where $\sqrt{s}$ is the e^+e^- c.m. energy. The generated events are subjected to detailed detector simulation based on GEANT4 [10], and are reconstructed with the software chain used for the experimental data. Temporal variations in the detector performance and beam background conditions are taken into account.

The processes with a J/ψ in the final state (Fig. 2), with J/ψ decaying into $\eta_c\gamma$, can imitate the process under study. The initial state radiation (ISR) process [Fig. 2(a)] contributes to the no-tag mode, while the J/ψ bremsstrahlung process [Fig. 2(b)] contributes background to the single-tag mode. We simulate both processes with J/ψ decaying to $K_S K^\pm \pi^\mp$ and also to $\eta_c\gamma$ followed by $\eta_c \rightarrow K_S K^\pm \pi^\mp$. To estimate a possible background from other two-photon processes we simulate the reaction $e^+e^- \rightarrow e^+e^-\eta_c\pi^0$. These events are generated with an isotropic distribution of the final-state mesons in the $\eta_c\pi^0$ rest frame.

III. EVENT SELECTION

We select $e^+e^- \rightarrow e^+e^-\eta_c$ candidates in the no-tag and single-tag modes, with zero and one detected electron, respectively. The decay mode $\eta_c \rightarrow K_S K^\pm \pi^\mp$ ($K_S \rightarrow \pi^+\pi^-$) is used to reconstruct η_c meson candidates.

Events are selected with at least four (five for single-tag mode) charged-particle tracks. Since a significant fraction of events contain beam-generated spurious track and photon candidates, one extra track and any number of extra photons are allowed in an event. The tracks corresponding to the charged kaon and pion must be oppositely charged, and must extrapolate to the interaction region. The kaon is

required to be positively identified, while the pion track is required to be inconsistent with the kaon hypothesis.

The track identified as an electron must originate from the interaction region and be in the polar angle range $0.387 < \theta < 2.400$ in the lab frame (0.64–2.69 in the e^+e^- c.m. frame). The latter requirement is needed for good electron identification. To recover electron energy loss due to bremsstrahlung, both internal and in the detector material before the DCH, the energy of any EMC shower close to the electron direction is combined with the measured energy of the electron track. The resulting c.m. energy of the electron candidate must be greater than 1 GeV.

A K_S candidate is formed from a pair of oppositely charged tracks fitted to a common vertex, and yielding an invariant mass value in the range 487.5–507.5 MeV/c^2, when the charged-pion mass is assigned to each track. The candidate is then refitted with a K_S mass constraint to improve the precision of its momentum measurement. To suppress combinatorial background, the angle between the K_S candidate momentum and the line connecting its production and decay vertices (ψ_{K_S}) is required to satisfy $\cos\psi_{K_S} > 0.95$.

An η_c candidate is formed from K_S, $K^\pm$, and $\pi^\mp$ candidates fitted to a common vertex. The preliminary selection criterion for no-tag events requires that $|\cos\theta_{\eta_c}^*| > 0.95$, where $\theta_{\eta_c}^*$ is the polar angle of the candidate η_c in the e^+e^- c.m. frame. Figure 3 shows the distribution of the invariant mass of the pions forming a K_S candidate ($M_{2\pi}$) for events satisfying this criterion. The shaded histogram demonstrates the effect of the requirement $\cos\psi_{K_S} > 0.95$. The transverse momentum of the η_c candidate in the e^+e^- c.m. frame is restricted to the range $p_\perp^* < 0.25$ GeV/c. The invariant mass distribution for η_c candidates is shown in Fig. 4, where for events with more than one η_c candidate (about 0.4% of signal events), the candidate with the smallest value of $p_\perp^*$ is selected. The η_c
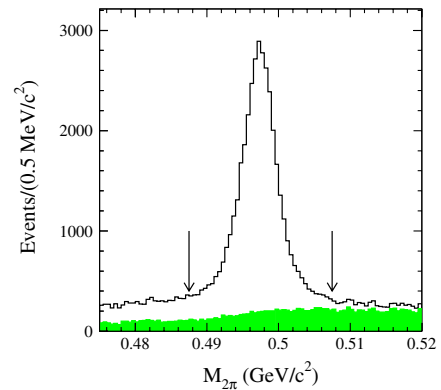

FIG. 3 (color online). The $M_{2\pi}$ distribution for K_S candidates in the no-tag data sample. The shaded histogram shows events rejected by the requirement $\cos\psi_{K_S} > 0.95$. The arrows indicate the region used to select event candidates.
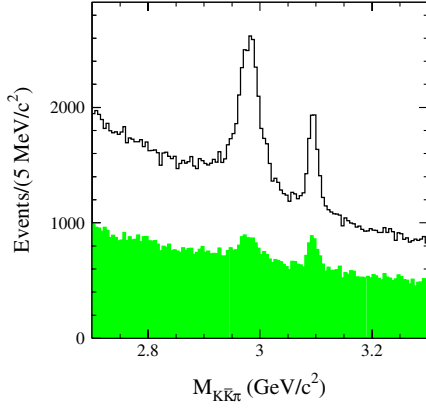
FIG. 4 (color online).   The distribution of the invariant mass of η_c candidates in the no-tag data sample. The shaded histogram shows events rejected by the requirement $p_\perp^* < 0.25$ GeV/c.

peak from two-photon production and the J/ψ peak from the ISR process $e^+e^- \rightarrow J/\psi\gamma$ are clearly seen in the invariant mass distribution. The shaded histogram shows the distribution for candidates rejected by the requirement $p_\perp^* < 0.25$ GeV/c. This requirement limits the momentum transfers to the electrons. The value of the effective threshold for q_i^2 ($i = 1, 2$) is determined from the dependence of the detection efficiency on $\max(-q_1^2, -q_2^2)$ and is about 0.1 GeV^2. Such a low q^2 threshold yields a model-independent extraction of $F(0, 0)$ from the no-tag data. We note that $d\sigma/dq_1^2 dq_2^2 \propto 1/(q_1^2 q_2^2)$ at small $|q_1^2|$ and $|q_2^2|$.

For single-tag events we combine an η_c candidate with an electron candidate and require $|\cos\theta_{e\eta_c}^*| > 0.95$, where $\theta_{e\eta_c}^*$ is the polar angle of the momentum vector of the $e\eta_c$ system in the e^+e^- c.m. frame. The transverse momentum of the $e\eta_c$ system is restricted to $p_\perp^* < 0.25$ GeV/c. The $p_\perp^*$ distribution for data candidates is shown in Fig. 5, where the shaded histogram is the corresponding distribution for simulated signal events. The condition on $p_\perp^*$

limits the value of the momentum transfer to the untagged electron (q_2^2). The effective q_2^2 threshold determined from simulation is about 0.1 GeV^2.

The emission of extra photons from the electrons involved leads to a difference between the measured and actual values of Q^2. In the case of ISR, $Q^2_{\mathrm{meas}} = Q^2_{\mathrm{true}}(1 + r_\gamma)$, where $r_\gamma = 2E_\gamma^*/\sqrt{s}$. To restrict the energy of the ISR photon we use the parameter

$$r = \frac{\sqrt{s} - E_{e\eta_c}^* - |p_{e\eta_c}^*|}{\sqrt{s}}, \qquad (3)$$

where $E_{e\eta_c}^*$ and $p_{e\eta_c}^*$ are the c.m. energy and momentum of the detected $e\eta_c$ system. In the ISR case this parameter coincides with r_γ defined above. The r distributions for data and simulated signal are shown in Fig. 6. Candidates with $-0.02 < r < 0.03$ are retained. We note that the condition on r ensures compliance with the restriction $r_\gamma < 0.1$ used in the MC simulation.

For two-photon events with a tagged positron (electron), the momentum of the detected $e\eta_c$ system in the e^+e^- c.m. frame has a negative (positive) z-component, while events resulting from e^+e^- annihilation are produced symmetrically. To suppress the e^+e^- annihilation background, event candidates with the wrong sign of the momentum z-component are removed.

The distribution of the invariant mass of η_c candidates for single-tag events satisfying the selection criteria described above is shown in Fig. 7. For events with more than one η_c candidate, the candidate with smallest $p_\perp^*$ is selected. Signals corresponding to η_c and J/ψ production are seen clearly in the mass spectrum. The J/ψ events are from the process $e^+e^- \rightarrow e^+e^- J/\psi$ [see Fig. 2(b)]. The shaded histogram in Fig. 7 shows the distribution for candidates with the wrong sign of the $e\eta_c$ momentum z-component. Since the numbers of events from e^+e^- annihilation in the wrong- and right-sign data samples
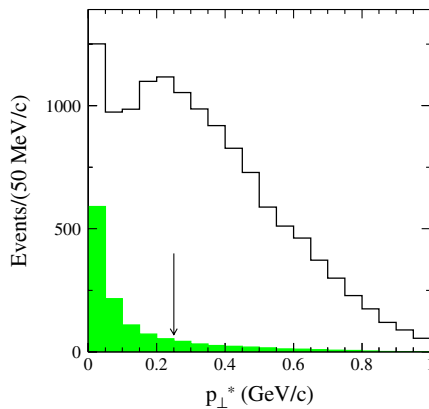

FIG. 5 (color online).   The transverse momentum distribution for $e\eta_c$ data candidates. The shaded histogram is for simulated signal events. Data candidates for which $p_\perp^* < 0.25$ GeV/c (indicated by the arrow) are retained.
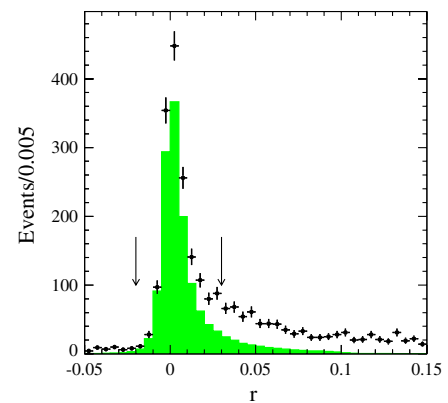

FIG. 6 (color online).   The distribution of r defined in Eq. (3) for data (points with error bars) and simulated signal events (shaded histogram). The arrows indicate the region used to select candidate events ($-0.02 < r < 0.03$).
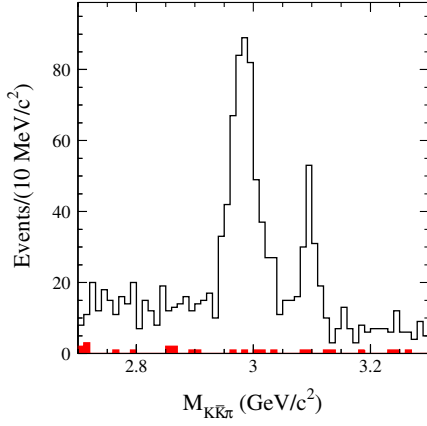
FIG. 7 (color online). The invariant mass distribution for single-tag η_c candidates. The shaded histogram is for events with the wrong sign of the $e\eta_c$ momentum z-component.
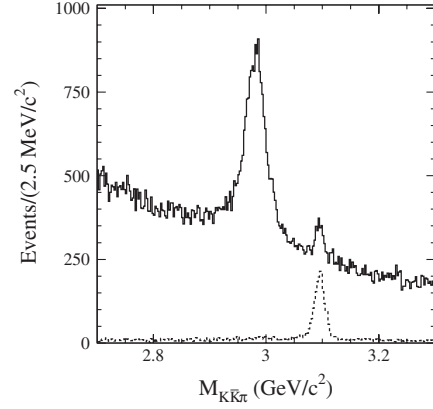

FIG. 8. The $K_S K^\pm \pi^\mp$ invariant mass spectrum for no-tag data events satisfying (dashed histogram) and not satisfying (solid histogram) the condition for ISR event selection [Eq. (4)].

are expected to be approximately the same, this shows that the background from e^+e^- annihilation peaking at the η_c mass is small.

IV. FITTING THE $K_S K^\pm \pi^\mp$ MASS SPECTRUM FOR NO-TAG EVENTS

The mass spectrum for no-tag events exhibits the η_c and J/ψ peaks corresponding to the two-photon and ISR production mechanisms, respectively. The c.m. momentum p^* of the $K_S K^\pm \pi^\mp$ system for ISR events is equal to $(\sqrt{s}/2) \times (1 - M_{K\bar{K}\pi}^2/s)$. In the mass region under study the detector acceptance strongly limits the efficiency for ISR events. Because of the asymmetry of the acceptance most of the detected ISR events have positive $\cos\theta_{\eta_c}^*$. It follows that the ISR events can be selected by requiring:

$$p^*/(1 - M_{K\bar{K}\pi}^2/s) > 5.1 \text{ GeV}/c, \qquad \cos\theta_{\eta_c}^* < 0. \quad (4)$$

The mass distribution for the events satisfying this condition is shown by dashed histogram in Fig. 8. The selected event sample contains mostly ISR events with very little two-photon η_c admixture. The $K_S K^\pm \pi^\mp$ mass distribution for the events not satisfying Eq. (4) is shown by the solid histogram in Fig. 8. The remaining J/ψ events are from the ISR process with more than one photon emitted from the initial state.

To determine the η_c mass and width, and the number of events containing an η_c, a binned likelihood fit is made to the distributions in Fig. 8 using a function consisting of signal (η_c and J/ψ) and background distributions. The bin size used in the fit is chosen to be 2.5 MeV/c^2. The J/ψ line shape is represented by the detector resolution function for ISR events. The η_c line shape is described by a Breit-Wigner function convolved with the detector resolution function corresponding to two-photon production. In each case, the detector resolution function is obtained using MC simulation of the detector response. We use

the nonrelativistic Breit-Wigner form

$$\frac{(\Gamma/2)^2}{(M_0 - M)^2 + (\Gamma/2)^2}, \quad (5)$$

where M is the $K_S K^\pm \pi^\mp$ invariant mass, and M_0 and Γ are the η_c mass and width. The changes in the values of the parameters, if a relativistic Breit-Wigner function is used, are negligible.

The detector resolution functions are determined from the distributions of the difference between measured and true simulated $K_S K^\pm \pi^\mp$ mass for the processes $e^+e^- \rightarrow e^+e^-\eta_c$, $\eta_c \rightarrow K_S K^\pm \pi^\mp$ and $e^+e^- \rightarrow J/\psi\gamma$, $J/\psi \rightarrow K_S K^\pm \pi^\mp$ shown in Figs. 9(a) and 9(b), respectively. The distributions are fit with the following function:

$$F(x) = A[G(x)\sin^2\zeta + B(x)\cos^2\zeta], \quad (6)$$

where

$$G(x) = \exp\left(-\frac{(x - a_1)^2}{2\sigma^2}\right), \quad (7)$$

$$B(x) = \begin{cases} \frac{(\Gamma_1/2)^{\beta_1}}{(a_2-x)^{\beta_1}+(\Gamma_1/2)^{\beta_1}} & \text{if } x < a_2; \\ \frac{(\Gamma_2/2)^{\beta_2}}{(x-a_2)^{\beta_2}+(\Gamma_2/2)^{\beta_2}} & \text{if } x \geq a_2, \end{cases} \quad (8)$$

A, ζ, a_1, σ, a_2, Γ_1, β_1, Γ_2, β_2 are free fit parameters. The $B(x)$ term is added to the Gaussian function to describe the asymmetric power-law tails of the δm distributions.

When used in data, the resolution σ in the Gaussian term of Eq. (6), is modified to take into account a possible difference between data and simulation:

$$\sigma^2 = \begin{cases} \sigma_{\text{MC}}^2 - \Delta\sigma^2 & \text{if } \Delta\sigma < 0; \\ \sigma_{\text{MC}}^2 + \Delta\sigma^2 & \text{if } \Delta\sigma \geq 0. \end{cases} \quad (9)$$

The parameter σ_{MC} is found to be 7.8 MeV/c^2 for the J/ψ and 7.6 MeV/c^2 for the η_c. The parameter $\Delta\sigma$ is determined from the fit to the measured $K_S K^\pm \pi^\mp$ mass spectra.
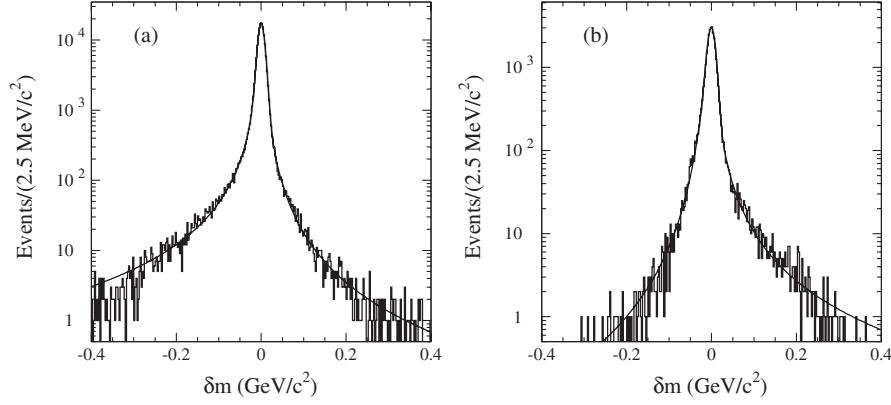
FIG. 9.   The distribution of the difference (δm) between measured and true $K_S K^{\pm} \pi^{\mp}$ mass for simulated events (a) for the two-photon process $e^+ e^- \rightarrow e^+ e^- \eta_c$, and (b) for the ISR process $e^+ e^- \rightarrow J/\psi \gamma$. The curves correspond to fits defined in the text.

The background distribution is described by a second-order polynomial. Both spectra shown in Fig. 8 are fit simultaneously with 14 free parameters: the J/ψ peak position ($m_{J/\psi}$), the difference between the J/ψ and η_c mass values (Δm), the η_c width (Γ), the numbers of η_c and J/ψ events, $\Delta\sigma$, and the background parameters for both spectra. The fitted curves are shown in Fig. 10. For the full mass range, 2.7–3.3 GeV/c^2, the χ^2 values corresponding to the η_c and J/ψ distributions (solid and dashed in Fig. 8) are 230 and 198, respectively, for a total number of degrees of freedom $2 \times 240 - 14$. The resulting parameter values are as follows:

$$\Delta m = 114.7 \pm 0.4 \text{ MeV}/c^2, \qquad \Gamma = 31.7 \pm 1.2 \text{ MeV},$$
$$N_{\eta_c} = 14450 \pm 320, \qquad \Delta\sigma = -0.4 \pm 2.5 \text{ MeV}/c^2,$$
$$m_{J/\psi} = 3095.8 \pm 0.3 \text{ MeV}/c^2. \tag{10}$$

The mass resolution for the J/ψ in data is found to be

consistent with the prediction of MC simulation. The fitted value of the J/ψ mass is shifted by -1.1 ± 0.3 MeV/c^2 from the nominal J/ψ mass value [7]. It is assumed that this mass scale shift does not affect the mass difference Δm. Since the momentum distributions for J/ψ and η_c events are different, and the MC simulation of the detector response is not perfect, we test this assumption as follows. The no-tag event sample was divided into three subsamples with approximately equal statistics but with different laboratory z momentum (p_z) of η_c candidates. The average p_z values in the subsamples are 3.2, -0.4, and -1.3 GeV/c, while the J/ψ momentum is peaked at $p_z = -2.34$ GeV/c. The fitted values of the Δm parameter for the three subsamples are found to be shifted relative to the nominal fit value by 0.5 ± 0.6, -0.6 ± 0.6, and 0.2 ± 0.6 MeV/c^2, respectively. We do not observe any significant dependence of the Δm parameter on the η_c momentum direction and absolute value. Nevertheless, the shift
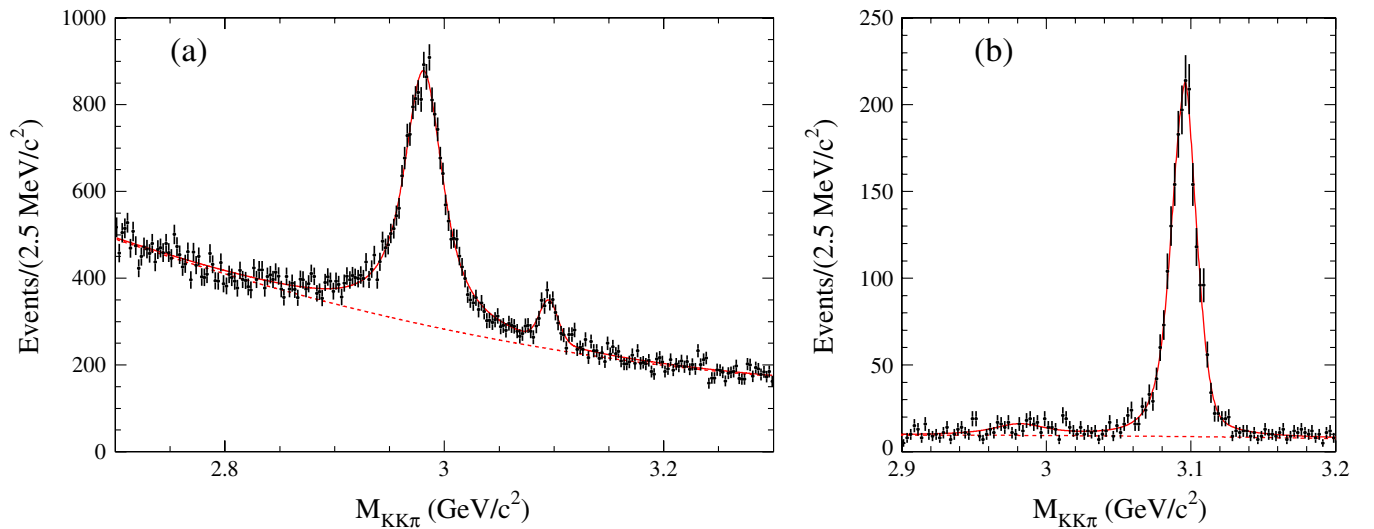

FIG. 10 (color online).   The $K_S K^{\pm} \pi^{\mp}$ invariant mass distribution and fitted curve for no-tag data events that (a) fail Eq. (4), and (b) satisfy Eq. (4) for ISR event selection.
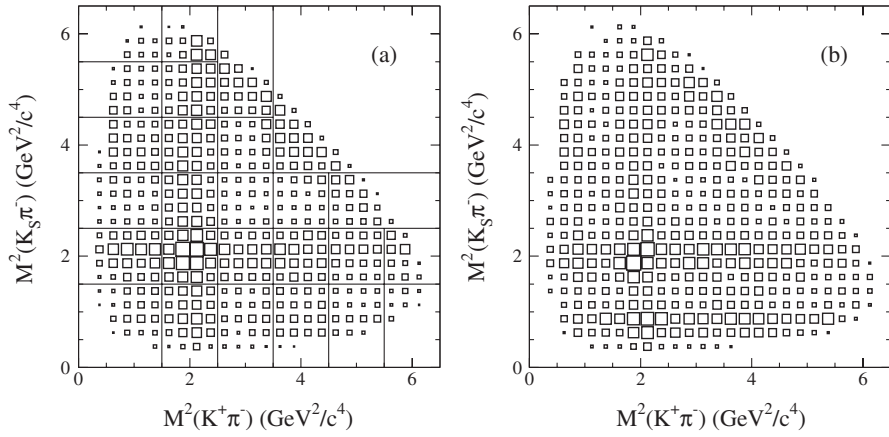
FIG. 11. The Dalitz plots for data events from (a) the η_c signal region $2.94 < M_{K\bar{K}\pi} < 3.02$ GeV/c^2, and (b) the combined sideband regions, $2.90 < M_{K\bar{K}\pi} < 2.94$ GeV/c^2 and $3.02 < M_{K\bar{K}\pi} < 3.06$ GeV/c^2.

value at the maximum difference between the η_c and J/ψ momenta, 0.5 MeV/c^2, is taken as an estimate of the Δm systematic uncertainty due to the difference of the J/ψ and η_c momentum distributions.

To estimate the uncertainty of the fit parameters due to the assumed background shape, the second-order polynomial describing background in Fig. 10(a) is replaced by an exponential function, and the changes in the parameter values are considered to be measures of their associated systematic uncertainties. This yields $\Delta\Gamma = 0.8$ MeV and $\Delta N_{\eta_c} = 400$.

The MC simulation uses a phase space distribution for $\eta_c \to K_S K^\pm \pi^\mp$ decay. This can lead to distortion of the resolution function and a systematic change in the detection efficiency determined from simulation. In order to address this issue, a study of the Dalitz plot distribution for $\eta_c \to K_S K^\pm \pi^\mp$ decay was performed. The Dalitz plots for data events from the η_c signal $(2.94 < M_{K\bar{K}\pi} <$ 3.02 GeV/c^2) and sideband $(2.90 < M_{K\bar{K}\pi} <$ 2.94 GeV/c^2 and $3.02 < M_{K\bar{K}\pi} < 3.06$ GeV/c^2) regions

are shown in Fig. 11, and their projections are shown in Fig. 12.

Figure 13 shows the distributions of $\cos\theta_K$, where θ_K is the charged-kaon polar angle in the $K_S K^\pm \pi^\mp$ rest frame, for events from the η_c region after background subtraction, and for events from the sidebands with the η_c contribution subtracted. The $\cos\theta_K$ distribution for η_c events closely resembles the distribution in the signal MC simulation shown by the dashed histogram in Fig. 13.

Since the MC simulation uses a phase space decay model, this suggests that in the $K_S K^\pm \pi^\mp$ mode the η_c decays predominantly via the scalar $K_0^*(1430)$ meson, i.e., $\eta_c \to K_0^*(1430)\bar{K}$.

It should be noted that a significant part of the non-η_c background comes from $\gamma\gamma \to K_S K^\pm \pi^\mp$, and so can interfere with the signal process $\gamma\gamma \to \eta_c \to K_S K^\pm \pi^\mp$. From the Dalitz plot, the background process seems to proceed mainly via the intermediate $K^*(892)\bar{K}$ and $K^*(1430)\bar{K}$ states, where the $K^*(1430)$ may be either the scalar [$K_0^*(1430)$) or tensor ($K_2^*(1430)$] state. Interference
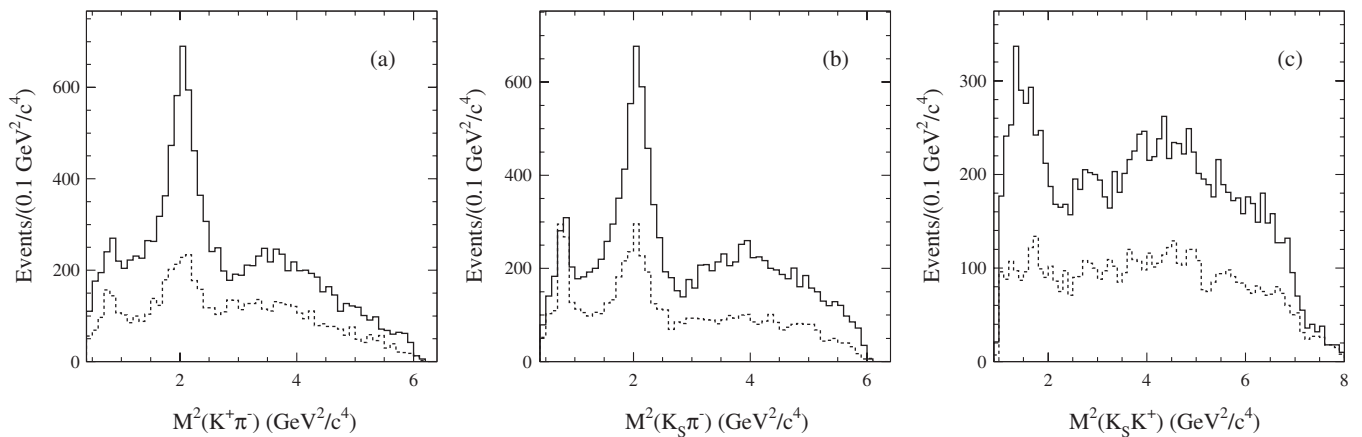

FIG. 12. The projections of the Dalitz plots of Fig. 11; the solid and dashed histograms correspond to the η_c signal and sideband $M_{K\bar{K}\pi}$ regions, respectively.
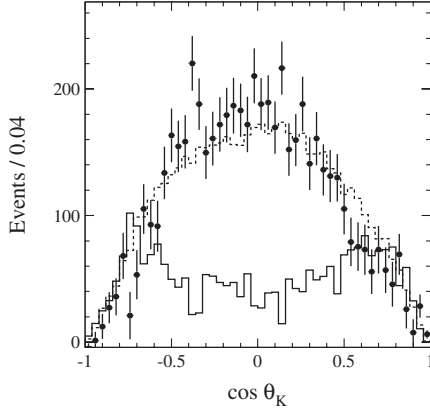
FIG. 13.   The $\cos\theta_K$ distribution for events from the η_c signal region after background subtraction (points with error bars), and for events from the sidebands after subtraction of the η_c contribution (solid histogram). The dashed histogram represents the signal MC simulation.

between the $I = 0$ and $I = 1$ background amplitudes appears to lead to the suppression of neutral $K^*(892)$ production [observed in Fig. 12(a) with respect to Fig. 12(b)]. The η_c signal distribution in Fig. 13 actually represents the $\cos\theta_K$ dependence of the detector acceptance. The $\cos\theta_K$ distribution for non-η_c events corrected for this acceptance will be peaked near ± 1. This means that the kaon in continuum is dominantly produced with large orbital momentum. Therefore, interference between the S-wave η_c decay amplitude and the $\gamma\gamma \rightarrow K_S K^{\pm} \pi^{\mp}$ nonresonant amplitude is expected to be small.

To estimate possible shifts of the η_c parameter values due to interference, an interference term is introduced into the fitting function through the following:

$$\left| \frac{\Gamma/2}{M_0 - M - i\Gamma/2} + A\sqrt{\frac{P_2(M)}{P_2(M_0)}} \right|^2, \qquad (11)$$

where the Breit-Wigner function describes the η_c amplitude, $P_2(M)$ is a second-order polynomial describing the mass dependence of the nonresonant intensity, and A is the value of this amplitude at the η_c mass. The $P_2(M)$ coefficients are chosen to be equal to the coefficients of the second-order polynomial describing the nonresonant background. A comparison of the Dalitz plot distributions for η_c and non-η_c events indicates that the maximal interference should occur in the vicinity of $M^2(K\pi) \approx 2 \text{ GeV2}/c^4$, where in both signal and background the quasi-two-body final states, $K_0^*(1430)\bar{K}$ and $\bar{K}_2^*(1430)\bar{K}$, dominate. Therefore, no significant phase shift is expected between the two amplitudes, and so parameter A is chosen to be real. From the fit, $A = 0.03 \pm 0.01$ and there are insignificant changes in the values of parameters Γ and N_{η_c}. The value of Δm changes by 1.5 MeV/c^2, and so this is considered to provide an estimate of the systematic uncertainty due to possible interference between the η_c and nonresonant amplitudes.

To take into account the difference between data and simulation of the $\eta_c \rightarrow K_S K^{\pm} \pi^{\mp}$ decay dynamics, the Dalitz plot is divided into 26 cells as shown in Fig. 11(a). For each cell the $K_S K^{\pm} \pi^{\mp}$ mass spectrum is fit using the fitting function described above, and the number of η_c events is determined. This experimental Dalitz plot distribution corrected for detection efficiency is used to reweight the signal simulation. The reweighting changes the resolution function and the fit parameter values insignificantly.

Thus, from the fit to the $K_S K^{\pm} \pi^{\mp}$ mass spectrum for no-tag events the following η_c parameter values are obtained:

$$\Delta m = 114.7 \pm 0.4 \pm 1.6 \text{ MeV}/c^2,$$

$$\Gamma = 31.7 \pm 1.2 \pm 0.8 \text{ MeV}, \qquad (12)$$

$$N_{\eta_c} = 14450 \pm 320 \pm 400.$$

When the nominal value of the J/ψ mass [7] is used, the η_c mass becomes $2982.2 \pm 0.4 \pm 1.6$ MeV/c^2. The results for the mass and width are in agreement with the previous *BABAR* measurement obtained using 88 fb^{-1} data [11]: $m_{\eta_c} = 2982.5 \pm 1.1 \pm 0.9$ MeV/c^2 and $\Gamma = 34.3 \pm 2.3 \pm 0.9$ MeV. The systematic uncertainty reported here is greater than that reported in the previous analysis as we are now allowing for the possibility that there exists a $J^P = 0^-$ continuum $K_S K^{\pm} \pi^{\mp}$ amplitude which interferes with the η_c amplitude.

V. FITTING THE $K_S K^{\pm} \pi^{\mp}$ MASS SPECTRUM FOR SINGLE-TAG EVENTS

The $K_S K^{\pm} \pi^{\mp}$ mass spectrum for single-tag events from data with $2 < Q^2 < 50$ GeV^2 is shown in Fig. 14. For $Q^2 > 50$ GeV^2 we do not see evidence of an η_c signal over background. To determine the number of η_c events, a binned likelihood fit is performed to the spectrum using a function consisting of a sum of η_c, J/ψ, and background distributions. The bin size used in the fit is chosen to be
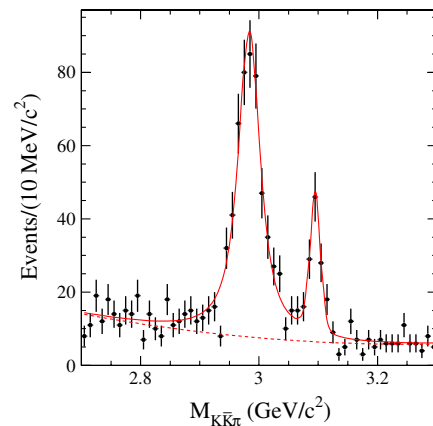

FIG. 14 (color online).   The $K_S K^{\pm} \pi^{\mp}$ mass spectrum for single-tag data events with $2 < Q^2 < 50$ GeV^2. The solid curve is the fit result. The dashed curve represents nonpeaking background.
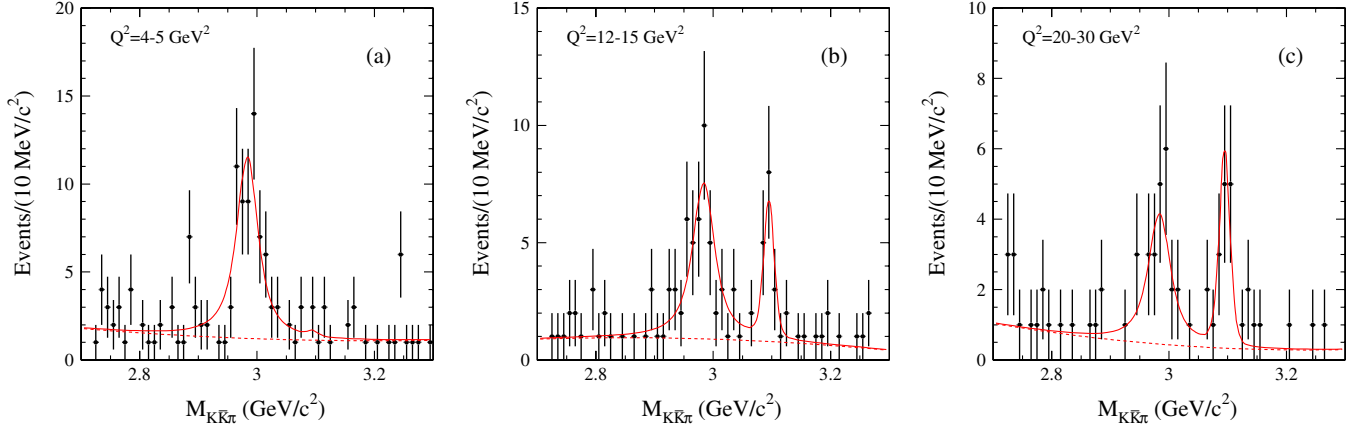
FIG. 15 (color online). The $K_S K^\pm \pi^\mp$ mass spectra for single-tag data events from three representative Q^2 intervals. In each figure the solid curve represents the fit result, and the dashed curve indicates nonpeaking background.

2.5 MeV/c^2. The mass resolution line shape is described by the function of Eq. (6) with parameters determined from the signal simulation reweighted to reproduce the Q^2 dependence observed in data. This resolution function and its convolution with a Breit-Wigner function are used to describe the J/ψ and η_c line shapes, respectively. The background distribution is described by either a second-order polynomial or an exponential function. The fit result is shown in Fig. 14 for a quadratic background. The fitted η_c parameter values, $\Delta m = 111.2 \pm 2.0$ MeV/c^2 and $\Gamma = 31.9 \pm 4.3$ MeV, are in agreement with the results obtained for no-tag events, and the total η_c signal is 530 ± 41 events. The difference in signal yield for the two background hypotheses is 17 events.

A fitting procedure similar to that described above is applied in each of the 11 Q^2 intervals indicated in Table I. The parameters of the mass resolution function are taken from the fit to the mass spectrum for simulated events in the corresponding Q^2 interval. The η_c and J/ψ masses are fixed at the values obtained from the fit to the spectrum of

Fig. 14, while the η_c width is taken from the fit to the no-tag data. The free parameters in the fit are the numbers of η_c and J/ψ events, and two or three additional parameters depending upon the description of the background shape (quadratic or exponential). The $K_S K^\pm \pi^\mp$ mass spectra and fitted curves (quadratic background) for three representative Q^2 intervals are shown in Fig. 15. The number of η_c events obtained from the fit using a quadratic background is listed for each Q^2 interval in Table I. The difference between the fit results for the two background hypotheses is used as an estimate of the systematic uncertainty associated with the assumed background form.

VI. PEAKING BACKGROUND ESTIMATION AND SUBTRACTION

Background containing true η_c's might arise from $e^+ e^-$ annihilation processes and two-photon processes with higher multiplicity final states. The processes with a J/ψ in the final state considered in previous sections are also

TABLE I. The Q^2 interval, number of events with η_c obtained from the fit (N_{η_c}), number of background events from $J/\psi \to \eta_c \gamma$ decay (N_{bkg}), efficiency correction (δ_{total}), and number of signal events corrected for data/MC difference and resolution effects ($N_{\mathrm{corr}}^{\mathrm{unfolded}}$). The quoted errors on N_{η_c} and $N_{\mathrm{corr}}^{\mathrm{unfolded}}$ are statistical and systematic.

Q^2 interval (GeV^2)	N_{η_c}	N_{bkg}	$\delta_{\mathrm{total}}(\%)$	$N_{\mathrm{corr}}^{\mathrm{unfolded}}$	$\varepsilon(\%)$
no-tag	$14450 \pm 320 \pm 400$	730 ± 240	-2.6	$14090 \pm 330 \pm 480$	14.5
2–3	$41.0 \pm 8.6 \pm 1.3$	0.7 ± 0.4	-0.1	$39.9 \pm 9.0 \pm 1.4$	2.0
3–4	$56.2 \pm 10.5 \pm 4.0$	0.6 ± 0.4	0.0	$55.3 \pm 10.9 \pm 4.2$	4.9
4–5	$65.0 \pm 10.9 \pm 1.1$	0.1 ± 0.4	-0.1	$64.8 \pm 11.5 \pm 1.2$	9.1
5–6	$52.6 \pm 9.6 \pm 0.6$	0.5 ± 0.4	-0.4	$51.8 \pm 10.3 \pm 0.8$	12.1
6–8	$90.9 \pm 12.2 \pm 4.6$	1.3 ± 0.8	-0.4	$90.3 \pm 12.8 \pm 4.9$	14.0
8–10	$60.9 \pm 10.9 \pm 2.8$	0.9 ± 0.6	-0.8	$61.3 \pm 11.7 \pm 3.1$	17.9
10–12	$34.8 \pm 7.3 \pm 1.8$	1.0 ± 0.6	-1.0	$33.5 \pm 7.9 \pm 2.1$	21.4
12–15	$42.3 \pm 8.7 \pm 2.1$	1.9 ± 0.8	-1.3	$41.2 \pm 9.4 \pm 2.4$	23.0
15–20	$45.5 \pm 7.9 \pm 1.0$	2.4 ± 1.0	-1.0	$44.3 \pm 8.5 \pm 1.5$	23.8
20–30	$23.7 \pm 6.6 \pm 0.6$	1.6 ± 0.7	-1.0	$22.5 \pm 6.9 \pm 1.0$	24.7
30–50	$10.8 \pm 4.5 \pm 0.1$	0.9 ± 0.5	-1.3	$10.3 \pm 4.8 \pm 0.5$	24.5

sources of peaking background because of the relatively large branching fraction for the decay $J/\psi \rightarrow \eta_c \gamma$ [7].

For no-tag events the most discriminating variable between signal and background is the η_c candidate transverse momentum ($p_\perp^*$). In particular it is expected that background from e^+e^- annihilation increases rapidly with transverse momentum. Figure 16 shows the $p_\perp^*$ distribution for no-tag data events containing an η_c. In each $p_\perp^*$ interval the number of η_c events is determined from the fit to the $K_S K^\pm \pi^\mp$ mass spectrum. It is seen that the data distribution is in good agreement with signal MC simulation. A conservative upper limit on the level of e^+e^- annihilation background is obtained by fitting a sum of the MC signal distribution and a constant background to the data $p_\perp^*$ distribution. The number of background events with $p_\perp^* < 0.25$ GeV/c is found to be 110 ± 150.

The two-photon background from the process $e^+e^- \rightarrow e^+e^- \eta_c \pi^0$ is studied using a special selection. From the sample of events satisfying preliminary selection criteria, events with two or more extra photons are selected with the energy of each photon required to be greater than 50 MeV. Two photons with total energy greater than 0.2 GeV, and invariant mass in the range 0.07–0.20 GeV/c^2 form a π^0 candidate. The π^0 candidate is combined with an η_c candidate, and it is required that the transverse momentum of the $\eta_c \pi^0$ system be less than 0.25 GeV/c. The resulting π^0 candidate mass spectrum is shown in Fig. 17, and the $K_S K^\pm \pi^\mp$ mass spectrum for events with $0.11 < M_{\gamma\gamma} < 0.15$ GeV/c^2 is shown in Fig. 18. The spectrum is fitted by a sum of signal (η_c and J/ψ) and background functions. The fitted number of η_c events is found to be 60 ± 40. Simulation of the $e^+e^- \rightarrow e^+e^- \eta_c \pi^0$ process shows that the ratio of the numbers of events selected using the standard and special criteria is about 2.5, so that the estimated background from $e^+e^- \rightarrow e^+e^- \eta_c \pi^0$ in the event sample with the standard selection is 150 ± 100. A similar approach is used to estimate a possible background from the $e^+e^- \rightarrow e^+e^- \eta_c \eta$ process. No η signal is observed in

FIG. 17. The π^0 candidate mass spectrum for the selected $e^+e^- \rightarrow e^+e^- K_S K^\pm \pi^\mp \pi^0$ data events in no-tag mode.

the two-photon mass spectrum, nor is there an η_c signal in the $K_S K^\pm \pi^\mp$ mass spectrum. The $e^+e^- \rightarrow e^+e^- \eta_c \eta$ background is therefore considered negligible.

Background from both sources, e^+e^- annihilation and two-photon processes, does not exceed 490 events (90% CL), i.e., 3.5% of the total number of η_c events. This number is considered to provide an estimate of the systematic uncertainty due to possible e^+e^- annihilation and two-photon background.

The total number of $e^+e^- \rightarrow J/\psi \gamma$, $J/\psi \rightarrow K_S K^\pm \pi^\mp$ events found in the no-tag event sample is 3170 ± 100. From simulation the ratio of the detection efficiencies $\varepsilon(e^+e^- \rightarrow J/\psi \gamma, J/\psi \rightarrow \eta_c \gamma, \eta_c \rightarrow K_S K^\pm \pi^\mp)/\varepsilon(e^+e^- \rightarrow J/\psi \gamma, J/\psi \rightarrow K_S K^\pm \pi^\mp)$ is found to be 1.18 ± 0.01. Taking into account the ratio of the branching fractions

$$b = \frac{\mathcal{B}(J/\psi \rightarrow \eta_c \gamma)\mathcal{B}(\eta_c \rightarrow K\bar{K}\pi)}{\mathcal{B}(J/\psi \rightarrow K\bar{K}\pi)} = 0.20 \pm 0.07$$
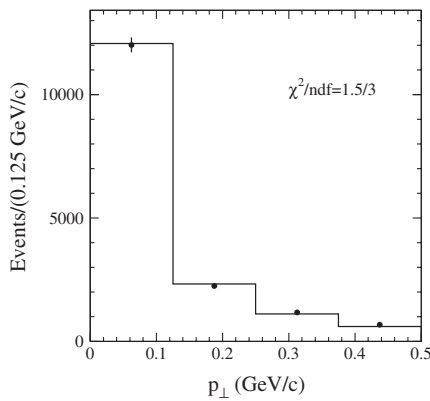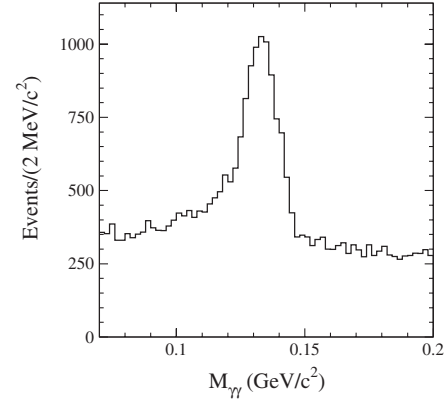
(13)

FIG. 16. The distribution of the η_c candidate transverse momentum for no-tag data events containing an η_c (points with error bars), and for simulated signal events (histogram).
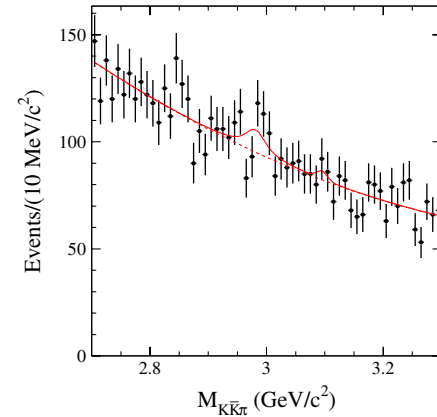

FIG. 18 (color online). The $K_S K^\pm \pi^\mp$ mass spectrum for $e^+e^- \rightarrow e^+e^- K_S K^\pm \pi^\mp \pi^0$ candidate events in no-tag mode with $0.11 < M_{\gamma\gamma} < 0.15$ GeV/c^2. The solid curve is the fit result. The dashed curve represents nonpeaking background.

the corresponding background contribution to the η_c peak from the ISR process is found to be 730 ± 240 events.

For single-tag events, the background from e^+e^- annihilation can be estimated using events with the wrong sign of the $e^{\pm}\eta_c$ momentum z-component. The $K_S K^{\pm}\pi^{\mp}$ mass spectrum for the wrong-sign events is shown in Fig. 7 together with the spectrum for right-sign events. Assuming that the numbers of background events for the wrong- and right-sign data samples are approximately the same, a fit to the mass spectrum for wrong-sign events yields 1.4 ± 3.0 e^+e^- annihilation events peaking at the η_c mass.

To estimate the two-photon background in the single-tag event sample, the result obtained for no-tag events is used. Assuming that the signal and background Q^2 dependences are approximately the same, it is estimated that the number of two-photon background events is 5.7 ± 3.0. The total background from e^+e^- annihilation and two-photon processes does not exceed 13 events (90% CL), or 2.5% of the total number of η_c events in the single-tag event sample. This number is considered to provide an estimate of the systematic uncertainty due to possible e^+e^- annihilation and two-photon background.

The background from the process $e^+e^- \to e^+e^- J/\psi$ [Fig. 2(b)], $J/\psi \to \eta_c \gamma$, $\eta_c \to K_S K^{\pm}\pi^{\mp}$ is estimated from the measured Q^2 distribution ($N_{J/\psi,i}$) for the $e^+e^- \to e^+e^- J/\psi, J/\psi \to K_S K^{\pm}\pi^{\mp}$ events as $\kappa_i b N_{J/\psi,i}$, where b is the ratio of the branching fractions defined in Eq. (13), and κ_i is the ratio of the detection efficiencies for the $J/\psi \to \eta_c\gamma$, $\eta_c \to K_S K^{\pm}\pi^{\mp}$ and $J/\psi \to K_S K^{\pm}\pi^{\mp}$ decay modes. The coefficient κ_i varies from 0.7 to 0.5 in the Q^2 range of interest. The estimated background contributions resulting from $J/\psi \to \eta_c\gamma$ decay are listed in Table I. The fraction of background in the $e^{\pm}\eta_c$ data sample changes from about 1.0% for $Q^2 < 10$ GeV^2 to about 5% at $Q^2 \approx 30$ GeV^2.

VII. DETECTION EFFICIENCY

The detection efficiency is determined from MC simulation as the ratio of the true Q^2 distributions computed after and before applying the selection criteria. The Q^2 dependence of the detection efficiency is shown in Fig. 19. The detector acceptance limits the detection efficiency at small Q^2. The cross section is measured in the region $Q^2 > 2$ GeV^2 where the detection efficiency is greater than 2%. The asymmetry of the e^+e^- collisions at PEP-II leads to different efficiencies for events with electron and positron tags. The Q^2 range from 2 to 6 GeV^2 is measured only with the positron tag. For no-tag events the detection efficiency is 0.1446 ± 0.0023. The efficiency is calculated using simulated events reweighted according to the Dalitz plot distribution observed in data. For no-tag events the relative difference between detection efficiencies calculated with and without weighting is found to be $-(1.1 \pm 1.6)\%$. The quoted error is determined by the statistical errors of the
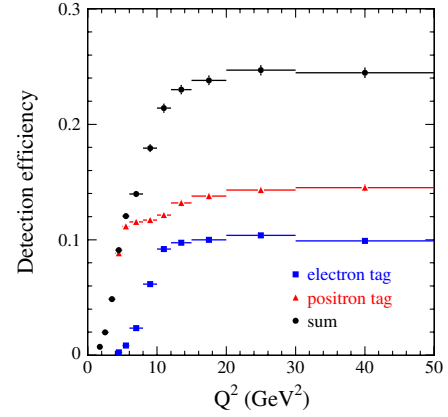

FIG. 19 (color online).   The detection efficiency as a function of momentum transfer squared for events with a tagged electron (squares), a tagged positron (triangles), and their sum (circles).

measured Dalitz plot distribution. The corresponding relative difference for single-tag events is shown in Fig. 20 as a function of Q^2. The detection efficiency has only a very weak dependence on the dynamics of η_c decay.

Possible sources of systematic uncertainty due to differences between data and simulated detector response are now considered. For no-tag events the MC simulation predicts a significant loss of signal events, $(5.3 \pm 0.1)\%$, due to background filters used in event reconstruction. The filter inefficiency can be measured in data using a special sample of prescaled events that does not pass the background filters. The filter inefficiency obtained in data is $(7.5 \pm 1.2)\%$. The difference $\delta = -(2.2 \pm 1.2)\%$ is used to correct the number of signal events. For single-tag events the presence of the additional electron leads to a significantly smaller filter inefficiency. The simulation predicts a filter inefficiency of $(0.57 \pm 0.02)\%$, which is about 10 times smaller than for no-tag events. We conclude that this source of systematic uncertainty is negligible for single-tag events.
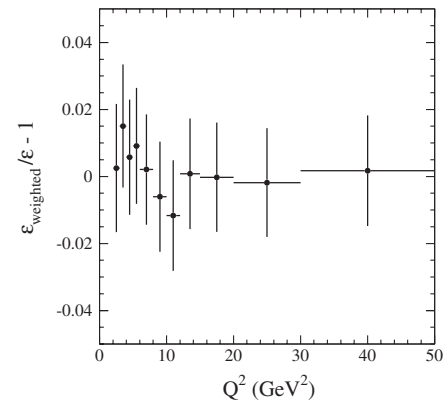

FIG. 20.   The Q^2 dependence of the relative difference between detection efficiencies determined from MC simulation with and without Dalitz-plot reweighting.

To study the possible systematics for no-tag events due to selection criteria, the mass window for the K_S candidate is increased from 487.5–507.5 MeV/c^2 to 475.0–520.0 MeV/c^2, the limit on the η_c candidate transverse momentum is changed from 0.25 to 0.50 GeV/c, and the polar angle restriction is set to $0.387 < \theta < 2.400$ rad for all four charged-particle tracks in an event. The last modification rejects about 30% of signal events. The double ratio

$$R_2 = \frac{(N_{\text{new}}/N)_{\text{data}}}{(N_{\text{new}}/N)_{\text{MC}}} \qquad (14)$$

is calculated, where N_{new} and N are the numbers of signal events with the new and standard selection criteria, and is found to be close to unity for the definition of the K_S mass window (0.993 ± 0.005), and for the condition on $p_\perp^*$ (1.002 ± 0.009). A significant deviation from unity (5.9 ± 1.8)% is observed for the polar angle restriction. This deviation is taken as an estimate of the systematic uncertainties due to imperfect simulation of the η_c selection criteria close to the limits of the fiducial tracking region.

The systematic uncertainty due to a possible difference between the data and simulation in the charged-particle track reconstruction for pions and kaons is estimated to be about 0.35% per track, so that the total uncertainty is estimated to be 1.4%. The data-MC simulation difference in the kaon identification is estimated using the identification efficiencies measured for kaons from the $D^{*+} \to D^0 \pi^+$, $D^0 \to \pi^+ K^-$ decay sequence. The efficiency correction is found to be -0.4%. The systematic uncertainty associated with this correction is taken to be equal to the value of the correction, 0.4%. The total efficiency correction for no-tag events is -2.6%, and the total systematic error associated with the efficiency is about 6.2%.

The polar angle restriction described above is also tested for single-tag events, and Fig. 21 shows the Q^2 dependence of the data-MC double ratio. No significant Q^2 dependence

FIG. 22. The correction to the MC-estimated kaon identification efficiency as a function of Q^2.

is observed, and the average value is 1.057 ± 0.032, which is very close to the value for no-tag events. For single-tag events the systematic uncertainty due to the η_c selection criteria is estimated to be 5.7%. The efficiency correction (δ_1) for kaon identification for single-tag events is shown in Fig. 22 as a function of Q^2, and this results in an associated systematic uncertainty of 0.5%.

The data-MC simulation difference in electron identification is estimated using the identification efficiencies measured for electrons from radiative Bhabha events. The efficiency correction (δ_2) is shown as a function of Q^2 in Fig. 23. The associated systematic uncertainty does not exceed 0.5%. The systematic uncertainty due to data-MC simulation difference in the electron track reconstruction is about 0.1%. To estimate the effect of the requirement $-0.02 < r < 0.03$ (see Fig. 6), events with $0.03 < r < 0.06$ are studied. The data-MC simulation double ratio defined by Eq. (14) is found to be consistent with unity, (0.99 ± 0.02), so that the simulation reproduces the shape of the r distribution very well.

The main sources of systematic uncertainty associated with detection efficiency are summarized in Table II for the
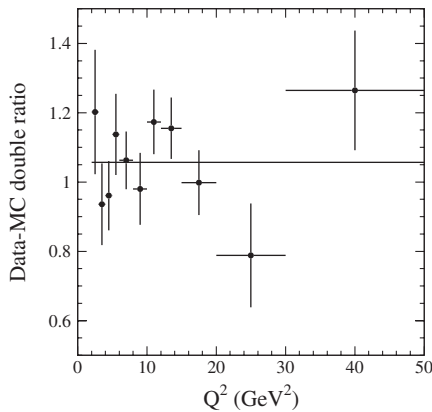

FIG. 21. The Q^2 dependence of the data-MC double ratio for events with and without the polar angle restriction $0.387 < \theta < 2.400$ rad for all four charged-particle tracks from the η_c decay.
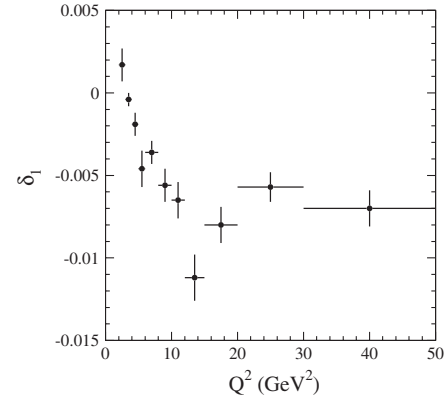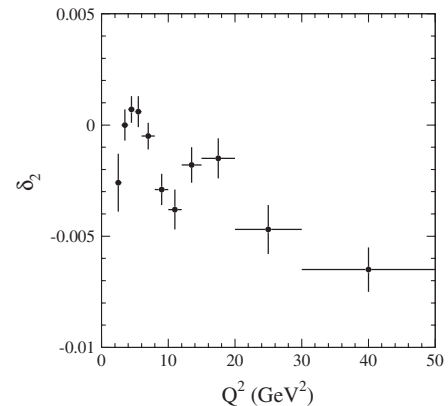

FIG. 23. The correction to the MC-estimated electron identification efficiency as a function of Q^2.

TABLE II. The main sources of systematic uncertainty associated with the detection efficiency and the total efficiency systematic error for no-tag and single-tag events.

Source	No tag, %	Single tag, %
trigger, filters	1.2	$\cdots$
η_c selection	5.9	5.7
track reconstruction	1.4	1.5
$K^\pm$ identification	0.4	0.5
$e^\pm$ identification	$\cdots$	0.5
total	6.2	5.9

FIG. 24. The Q^2 dependence of the radiative correction factor.

no-tag and single-tag samples. The values of the detection efficiency and total efficiency correction $\delta_{\mathrm{total},i} \approx \delta_{1,i} + \delta_{2,i}$ for different Q^2 intervals are listed in Table I. The data distribution is corrected as follows:

$$N_{\mathrm{corr},i} = N_i/(1 + \delta_{\mathrm{total},i}), \qquad (15)$$

where $N_i = N_{\eta_c,i} - N_{\mathrm{bkg},i}$ is the number of signal events in the ith Q^2 interval.

VIII. CROSS SECTION AND FORM FACTOR

The Born differential cross section for $e^+e^- \to e^+e^-\eta_c$, $\eta_c \to K\bar{K}\pi$ is

$$\frac{d\sigma}{dQ^2} = \frac{(dN/dQ^2)^{\mathrm{unfolded}}_{\mathrm{corr}}}{\varepsilon R L}$$

$$\times \frac{\mathcal{B}(\eta_c \to K\bar{K}\pi)}{\mathcal{B}(\eta_c \to K_S K^\pm \pi^\mp)\mathcal{B}(K_S \to \pi^+\pi^-)} \quad (16)$$

where $(dN/dQ^2)^{\mathrm{unfolded}}_{\mathrm{corr}}$ is the mass spectrum corrected for data-MC simulation difference and unfolded for detector resolution effects, explained below, L is the total integrated luminosity, ε is the Q^2-dependent detection efficiency, R is a radiative correction factor accounting for distortion of the Q^2 spectrum due to the emission of photons from the initial-state particles, and for vacuum polarization effects. The ratio $\mathcal{B}(\eta_c \to K\bar{K}\pi)/\mathcal{B}(\eta_c \to K_S K^\pm \pi^\mp)$ is expected to be 3 from isospin relations.

The radiative correction factor is determined using simulation at the generator level (with no detector simulation). The Q^2 spectrum is generated using only the pure Born amplitude for the $e^+e^- \to e^+e^-\eta_c$ process, and then using a model with radiative corrections included. The Q^2 dependence of the radiative correction factor, evaluated as the ratio of the second spectrum to the first, is shown in Fig. 24, and is fitted using the function $a/(1 + bQ^\gamma)$. The accuracy of the radiative correction calculation is estimated to be 1% [9]. It should be noted that the value of R depends on the requirement on the extra photon energy. The Q^2 dependence obtained corresponds to the condition $r = 2E_\gamma^*/\sqrt{s} < 0.1$ imposed in the simulation.

The corrected and unfolded Q^2 distribution $(dN/dQ^2)^{\mathrm{unfolded}}_{\mathrm{corr}}$ is obtained from the measured distribu-
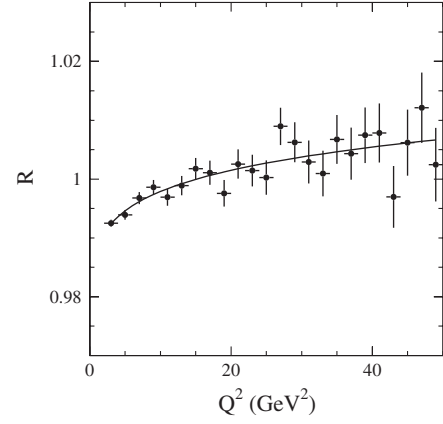
tion by dividing by the efficiency correction factor (see Eq. (15)) and unfolding the effect of Q^2 resolution. Using MC simulation, a migration matrix H is obtained, which represents the probability that an event with true Q^2 in interval j be reconstructed in interval i:

$$\left(\frac{dN}{dQ^2}\right)^{\mathrm{rec}}_i = \sum_j H_{ij}\left(\frac{dN}{dQ^2}\right)^{\mathrm{true}}_j. \qquad (17)$$

In the case of extra photon emission, Q^2_{true} is calculated as $-(p - p' - k)^2$, where k is the photon four-momentum; ε and R in Eq. (16) are functions of Q^2_{true}. As the chosen Q^2 interval width significantly exceeds the resolution for all Q^2, the migration matrix is nearly diagonal, with values of diagonal elements ~ 0.95, and of the next-to-diagonal ~ 0.02. The true Q^2 distribution is obtained by applying the inverse of the migration matrix to the measured distribution. The procedure changes the shape of the Q^2 distribution insignificantly, but increases the errors (by $\approx 10\%$) and their correlations. The corrected Q^2 spectrum ($N^{\mathrm{unfolded}}_{\mathrm{corr}}$) is listed in Table I.

The values of the differential cross sections obtained are listed in Table III, where the first error is statistical and the second systematic. The latter includes only Q^2-dependent errors, namely, the systematic uncertainty in the number of signal events and the statistical errors on the efficiency correction and MC simulation. The Q^2-independent systematic error is 6.6%; this results from the systematic uncertainties on the detection efficiency (5.9%), background subtraction (2.5%), the radiative correction factor (1%), and the error on the integrated luminosity (1%) combined in quadrature. The MC simulation for single-tag events is performed, and the detection efficiency is determined, with the restriction that the momentum transfer to the untagged electron be greater than -1 GeV^2, so that the cross section is measured for the restricted range $|q^2| < 1$ GeV^2. The measured differential cross section is shown in Fig. 25.

Because of the strong nonlinear dependence of the cross section on Q^2, the value of Q^2 corresponding to the mea-

TABLE III.   The Q^2 interval and the weighted average Q^2 value ($\overline{Q^2}$), the $e^+e^- \to e^+e^- \eta_c$ cross section multiplied by $\mathcal{B}(\eta_c \to K\bar{K}\pi)$ [$d\sigma/dQ^2(\overline{Q^2})$], and the normalized $\gamma\gamma^* \to \eta_c$ transition form factor ($|F(\overline{Q^2})/F(0)|$). The statistical and systematic errors are quoted separately for the cross section, but are combined in quadrature for the form factor. Only Q^2-dependent systematic errors are quoted; the Q^2-independent error is 6.6% for the cross section and 4.3% for the form factor.

Q^2 interval (GeV^2)	$\overline{Q^2}$ (GeV^2)	$d\sigma/dQ^2(\overline{Q^2})$ (fb/GeV^2)	$|F(\overline{Q^2})/F(0)|$
2–3	2.49	$18.7 \pm 4.2 \pm 0.8$	0.740 ± 0.085
3–4	3.49	$10.6 \pm 2.1 \pm 0.8$	0.680 ± 0.073
4–5	4.49	$6.62 \pm 1.18 \pm 0.19$	0.629 ± 0.057
5–6	5.49	$4.00 \pm 0.80 \pm 0.10$	0.555 ± 0.056
6–8	6.96	$3.00 \pm 0.43 \pm 0.17$	0.563 ± 0.043
8–10	8.97	$1.58 \pm 0.30 \pm 0.08$	0.490 ± 0.049
10–12	10.97	$0.72 \pm 0.17 \pm 0.05$	0.385 ± 0.048
12–15	13.44	$0.55 \pm 0.13 \pm 0.03$	0.395 ± 0.047
15–20	17.35	$0.34 \pm 0.07 \pm 0.01$	0.385 ± 0.038
20–30	24.53	$0.084 \pm 0.026 \pm 0.004$	0.261 ± 0.041
30–50	38.68	$0.019 \pm 0.009 \pm 0.001$	0.204 ± 0.049

sured cross section differs slightly from the center of the Q^2 interval. The measured cross section is described by a smooth function, which is then used to reweight the simulated Q^2 distribution and calculate the weighted average value ($\overline{Q^2}$) for each Q^2 interval. The values of $\overline{Q^2}$ obtained are listed in Table III.

The no-tag event sample is used to obtain the total cross section for the reaction $e^+e^- \to e^+e^- \eta_c$, $\eta_c \to K\bar{K}\pi$:

$$\sigma_{\text{total}} = \frac{N_{\text{corr}}}{\varepsilon L} \frac{\mathcal{B}(\eta_c \to K\bar{K}\pi)}{\mathcal{B}(\eta_c \to K_S K^\pm \pi^\mp)\mathcal{B}(K_S \to \pi^+ \pi^-)}. \tag{18}$$

In the no-tag mode the radiative correction is expected to be less than 1% [12], and so the associated systematic uncertainty is assigned conservatively as 1%. Taking N_{corr} and ε from Table I, the value obtained from
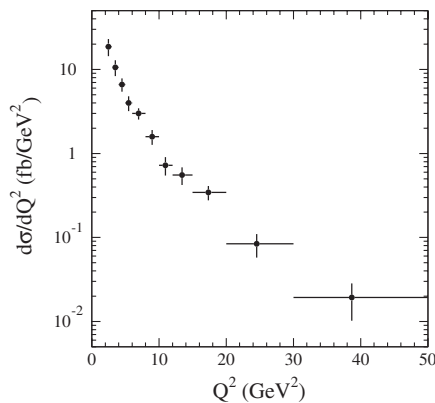

FIG. 25.   The $e^+e^- \to e^+e^- \eta_c$ differential cross section multiplied by the $\eta_c \to K\bar{K}\pi$ branching fraction; the statistical and Q^2-dependent systematic errors of Table III have been combined in quadrature.

Eq. (18) is

$$\sigma_{\text{total}} = 0.900 \pm 0.021 \pm 0.074 \text{ pb}. \tag{19}$$

The quoted errors are statistical and systematic, respectively. The latter is 8.1% and includes the systematic uncertainty in the number of signal events (3.3%), the statistical and systematic errors on the detection efficiency (1.6% and 6.2%, respectively), on the background subtraction (3.5%), on the radiative correction (1%), and the error on the integrated luminosity (1%). Using MC simulation, the calculated total cross section corresponding to $\Gamma(\eta_c \to \gamma\gamma)\mathcal{B}(\eta_c \to K\bar{K}\pi) = 1$ keV is found to be 2.402 pb, and hence from Eq. (19) the value

$$\Gamma(\eta_c \to \gamma\gamma)\mathcal{B}(\eta_c \to K\bar{K}\pi)$$
$$= 0.374 \pm 0.009 \pm 0.031 \text{ keV} \tag{20}$$

is obtained. This result agrees with the Particle Data Group value 0.44 ± 0.05 keV [7], and also with the recent CLEO measurement $0.407 \pm 0.022 \pm 0.028$ keV [13].

To extract the transition form factor, the measured and calculated Q^2 spectra are compared. The simulation for single-tag events uses a constant form factor value, so that the measured normalized form factor is determined from

$$|F^2(Q^2)/F^2(0)| = \frac{(dN/dQ^2)^{\text{data}}_{\text{single-tag}}}{N^{\text{data}}_{\text{no-tag}}}$$
$$\times \frac{\varepsilon_{\text{no-tag}}\sigma^{\text{MC}}_{\text{total}}}{\varepsilon_{\text{single-tag}}(Q^2)(d\sigma/dQ^2)^{\text{MC}}_{\text{single-tag}}}. \tag{21}$$

The normalized form factor is proportional to the ratio of the number of single-tag events to the number of no-tag events. It is expected that part of the systematic uncertainty, in particular, that associated with the detection

efficiency, cancels in this ratio. However, the single-tag data sample is not large enough for a detailed study of the Q^2-dependence of the observed data-MC simulation difference in detector response. Therefore, this uncertainty is estimated conservatively to be equal to the corresponding systematic uncertainty for the single-tag events (6%). The values of the form factor obtained are listed in Table III, and shown in Fig. 26, with the statistical and Q^2-dependent systematic errors combined. The Q^2-independent systematic error on the form factor is 4.3%; this value combines in quadrature the systematic uncertainty on detection efficiency, the uncertainty on the number of no-tag events, the statistical error on the detection efficiency for no-tag events, the uncertainties associated with the background subtraction, and the uncertainty on the radiative correction.

The form factor data of Fig. 26 are well described by the monopole form

$$|F(Q^2)/F(0)| = \frac{1}{1 + Q^2/\Lambda}, \qquad (22)$$

as shown by the solid curve. The corresponding fitted value of the pole parameter Λ is

$$\Lambda = 8.5 \pm 0.6 \pm 0.7 \text{ GeV}^2, \qquad (23)$$

where the second quoted error is due to the 4.3% Q^2-independent systematic error on the measurements. This value of the pole parameter is in reasonable agreement with that expected from vector dominance, namely $\Lambda = m_{J/\psi}^2 = 9.6 \text{ GeV}^2$, and in good agreement with the lattice QCD calculation, $\Lambda = 8.4 \pm 0.4 \text{ GeV}^2$ [5]. The dotted curve in Fig. 26 shows the result of the leading-order pQCD calculation of Ref. [3]. The data lie systematically below this prediction, but within the theoretical uncertainty quoted in Ref. [3].
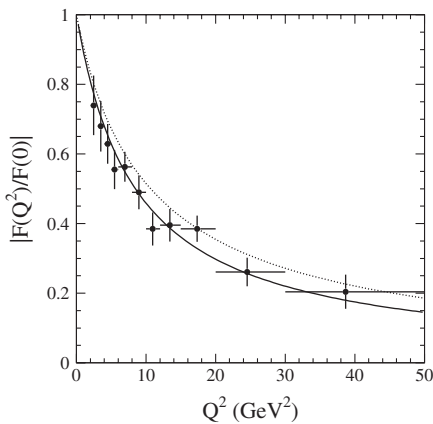

FIG. 26. The $\gamma\gamma* \to \eta_c$ transition form factor normalized to $F(0)$ (points with error bars). The solid curve shows the fit to Eq. (22). The dotted curve shows the leading order pQCD prediction from Ref. [3].

IX. SUMMARY

The reaction $e^+e^- \to e^+e^- \eta_c$, with $\eta_c \to K_S K^\pm \pi^\mp$, has been studied in the no-tag and single-tag modes. We measure the following values for the η_c mass and width:

$$m_{\eta_c} = 2982.2 \pm 0.4 \pm 1.6 \text{ MeV}/c^2,$$
$$\Gamma = 31.7 \pm 1.2 \pm 0.8 \text{ MeV}. \qquad (24)$$

These results agree with earlier *BABAR* measurements [11] and supersede them.

We have also measured the total cross section $\sigma(e^+e^- \to e^+e^- \eta_c)\mathcal{B}(\eta_c \to K\bar{K}\pi)$ and differential cross section $(d\sigma/dQ^2)\mathcal{B}(\eta_c \to K\bar{K}\pi)$. From these data we determine the value

$$\Gamma(\eta_c \to \gamma\gamma)\mathcal{B}(\eta_c \to K\bar{K}\pi)$$
$$= 0.374 \pm 0.009 \pm 0.031 \text{ keV} \qquad (25)$$

and measure the normalized $\gamma\gamma* \to \eta_c$ transition form factor $|F(Q^2)/F(0)|$ for the momentum transfer range from 2 to 50 GeV^2. The latter is well described by the simple monopole form of Eq. (22) with $\Lambda = 8.5 \pm 0.6 \pm 0.7 \text{ GeV}^2$ in agreement with both the vector dominance expectation and the QCD prediction.

[1] S. J. Brodsky, T. Kinoshita, and H. Terazawa, Phys. Rev. D **4**, 1532 (1971).

[2] G. P. Lepage and S. J. Brodsky, Phys. Rev. D **22**, 2157 (1980).

[3] T. Feldmann and P. Kroll, Phys. Lett. B **413**, 410 (1997).

[4] F. G. Cao and T. Huang, Phys. Rev. D **59**, 093004 (1999).

[5] J. J. Dudek and R. G. Edwards, Phys. Rev. Lett. **97**, 172001 (2006).

[6] M. Acciarri *et al.* (L3 Collaboration), Phys. Lett. B **461**, 155 (1999).

[7] C. Amsler *et al.* (Particle Data Group), Phys. Lett. B **667**, 1 (2008); 2009 partial update for the 2010 edition, http://pdg.lbl.gov.

[8] B. Aubert *et al.* (*BABAR* Collaboration), Nucl. Instrum. Methods Phys. Res., Sect. A **479**, 1 (2002).

[9] S. Ong and P. Kessler, Phys. Rev. D **38**, 2280 (1988).

[10] S. Agostinelli *et al.* (GEANT4 Collaboration), Nucl. Instrum. Methods Phys. Res., Sect. A **506**, 250 (2003).

[11] B. Aubert *et al.* (*BABAR* Collaboration), Phys. Rev. Lett. **92**, 142002 (2004).

[12] M. Defrise, S. Ong, J. Silva, and C. Carimalo, Phys. Rev. D **23**, 663 (1981); W. L. van Neerven and J. A. M. Vermaseren, Nucl. Phys. **B238**, 73 (1984).

[13] D. M. Asner *et al.* (CLEO Collaboration), Phys. Rev. Lett. **92**, 142001 (2004).